Engineering POLYTAC Nanoparticles for Bioorthogonal Click Reaction-Enforced Protein Degradation and Breast Cancer Therapy

Haijun Yu (hjyu@simm.ac.cn)
Shanghai Institute of Materia Medica, CAS https://orcid.org/0000-0002-3398-0880
jing gao
Qiwen Zhu
Shanghai Institute of Materia Medica, CAS
Bo Hou
Shanghai Institute of Materia Medica, CAS
Lei Yang
Nanjing University of Chinese Medicine
Xingyu Jiang
Nanjing University of Chinese Medicine
Zhifeng Zou
Shanghai Institute of Materia Medica, CAS
Xutong Li
Shanghai Institute of Materia Medica, CAS
Zhiai Xu
East China Normal University
Tianfeng Xu
Shanghai Institute of Materia Medica, CAS
Mingyue Zheng
Shanghai Institute of Materia Medica https://orcid.org/0000-0002-3323-3092
Huixiong Xu
Tongji University

Article

Keywords: Polymeric PROTAC, Bioorthogonal reaction, Prodrug nanoparticles, Tumor microenvironment, Combinatory therapy

Posted Date: February 10th, 2022

DOI: https://doi.org/10.21203/rs.3.rs-1197718/v1

Version of Record: A version of this preprint was published at Nature Communications on July 26th, 2022. See the published version at https://doi.org/10.1038/s41467-022-32050-4.

Abstract

PROteolysis TArgeting Chimeras (PROTACs) have been extensively explored for targeted protein degradation and cancer therapy. However, clinic translation of the conventional small molecular PROTACs is challenged by their unfavorable pharmacokinetic profiles and the systemic toxicity due to on-target but off-tumor protein degradation. Herein we presented a tumor microenvironment-activatable polymeric PROTAC (namely POLYTAC) nanoplatform for tumor-specific PROTAC delivery and combinatory cancer therapy. The POLYTAC nanoparticles were engineered by integrating metalloproteinase-liable poly(ethylene glycol) shell, intracellular acidity-responsive hydrophobic core and reduction-activatable PROTACs into one nanoplatform. The resultant POLYTAC nanoparticles can specifically accumulate at the tumor site and release the PROTACs inside the tumor cells for protein degradation. The POLYTAC nanoparticles can be further engineered for bioorthogonal click reaction-enforced tumor-specific delivery of the PROTACs. In combination with photodynamic therapy, we demonstrated that the bioorthogonal POLYTAC nanoparticles remarkably suppressed tumor growth by synergistically inducing cellular apoptosis of the tumor cells in mouse model of MDA-MB-231 breast cancer. The POLYTAC approach might pave the way for tumor-targeted protein degradation and translation of PROTAC-based cancer therapy.

Introduction

The heterobifunctional PROteolysis TArgeting Chimeras (PROTACs) hold promising potential for cancer therapy by degrading the onco-proteins, in particular the undruggable target[1–3]. PROTACs are generally composed of a “warhead” binding the protein of interest (POI), a ligand hijacking endogenous E3 ubiquitin ligase, and the linker connecting the warhead and the ligand[4–6]. PROTAC can label the POI with ubiquitin by recognizing the E3 ligase and subsequently, degrade the POI with the ubiquitin-proteasome system (UPS)[7–9]. Compared to the small molecular inhibitors, PROTAC can potentially degrade any intracellular proteins, including those undruggable targets (e.g., transcriptional factors and scaffold proteins)[10–12]. Furthermore, PROTACs are potent for circumventing acquired drug resistance via degrading whole proteins with low drug exposure time and dosage[13–14]. Despite promising, the conventional small molecular PROTACs generally display unfavorable pharmacokinetics and lack of tumor specificity, which might cause systemic toxicity due to their non-specific distribution in the normal tissues[15–16]. It remains a formidable challenge to achieve tumor-specific delivery and potentiate the antitumor potency of the conventional PROTACs.

To achieve tumor-targeted delivery of the PROTACs, several ligand-modification strategies (e.g., antibody-PROTACs, folate-PROTAC and Aptamer-PROTAC conjugates) have been investigated in past years[17–22]. With the assistance of these ligand “gunsight”, the decorated PROTACs showed increased cellular uptake in the tumor cells *in vitro*. In particular, the Aptamer-PROTAC conjugates displayed increased tumor accumulation and antitumor potency than the conventional PROTACs. Nevertheless, these ligand-PROTAC conjugates suffer from low serum stability, limited tumor penetration and heterogeneous

expression of the receptors in different tumor cells and cancer types. Furthermore, opto-PROTACs were developed for ultraviolet light-inducible protein degradation[23–24]. These photo-activatable PROTACs were demonstrated for spatiotemporally controllable protein degradation *in vitro*. However, clinical translation of the opto-PROTACs was restricted by the poor tissue penetration profile of the ultraviolet light. Therefore, precise PROTACs delivery to the tumor and efficient POI degradation inside the tumor cells remains a formidable challenge.

To this end, we proposed a rationally-designed polymeric PROTAC (POLY-PROTAC) nanotherapeutic for tumor-targeted delivery of the conventional PROTACs and degradation of bromodomain and extraterminal (BET) protein BRD4. The POLY-PROTAC nanoparticles (NPs) were engineered by utilizing the extracellular and intracellular signals (e.g., acidity, enzyme, and reduction) in the tumor microenvironment[25–27]. We first synthesized four VHL-based RPOTACs for BRD4 degradation, and then prepared a series of POLY-PROTACs by reversible addition-fragmentation chain transfer (RAFT) copolymerization approach. The amphiphilic POLY-PROTACs were self-assembled into micellar NPs for systemic delivery of the BRD4 PROTACs (Fig. 1A). To enforce tumor specificity of the POLY-PROTAC, an extracellular tumor acidity (i.e., pH = 6.5 ~ 6.8)-activatable pretargeted NP was subsequently engineered for tumor-specific delivery of dibenzocyclooctyne (DBCO) groups. The azide-modified POLY-PROTAC NPs were thus trapped inside the extracellular matrix of the tumor via in-situ click reaction between the DBCO and azide derivatives. The POLY-PROTAC NPs can be relieved in the tumor mass via extracellular matrix metalloproteinase-2 (MMP-2)-mediated cleavage of the PEG corona. Upon internalization into the tumor cells, the POLY-PROTAC NPs were dissociated inside the acidic endocytic vesicles (i.e., pH = 5.5 ~ 6.5), and released the PROTAC payload via GSH-mediated reduction of the disulfide bond (Fig. 1B). We further demonstrated that the clickable POLY-PROTAC NPs synergistically induced apoptosis of the tumor cells in combination with photodynamic therapy (PDT) in a mouse model of MDA-MB-231 breast cancer (Fig. 1C). This study might provide a generalizable POLY-PROTAC nanoplatform for tumor-specific PROTAC delivery and potentiated cancer therapy.

Synthesis And Characterization Of The Poly-protac Nps

The BET family proteins, in particular BRD4, have been investigated as promising antitumor targets due to their crucial role for gene transcription[28]. To design the BRD4-targeted POLY-PROTAC, we selected von Hipel-Lindau (VHL) ligand for PROTAC synthesis since the hydroxyl group in VHL can be reversibly caged via a disulfide spacer. The VHL protein binding ability of the modified PROTACs can be restored by GSH-triggered cleavage of the disulfide bond in the cytosol of tumor cells.

We first synthesized four VHL-based PROTACs by adjusting chemical structures of the VHL ligand and linkers (Fig. 2A, Supplementary Scheme 1-4 and Figs. 1-11). Western blot assay validated that all the four PROTACs remarkably degraded BRD4 in MDA-MB-231 breast cancer cells *in vitro*, and consequently suppressed downstream c-Myc expression. Noticeably, compounds ARV771 and MZ1 more efficiently reduced BRD4 expression compared to their analogs. The half-degradation concentration (DC_{50}) of ARV771 was 1.9-fold lower than that of mARV771 (Figs. 2B, C and Supplementary Fig. 12). CCK-8 assay

displayed that all four PROTACs comparably inhibited proliferation of MDA-MB-231 cells. Of note, the half inhibition concentration (IC_{50}) of the PROTACs were tens of times lower the BRD4 inhibitor JQ1 (Fig. 2D), suggesting BRD4 degrader more significantly impaired proliferation of the tumor cells than BRD4 inhibitor.

Molecular docking revealed that the hydroxyl in the VHL ligand form H-bond with HIE-115 and SER-111 in the binding pocket of VHL protein (Fig. 2E), verifying the crucial role of hydroxyl group for VHL protein binding. The hydroxyl group of ARV771 and MZ1 was thus methacrylated with a disulfide spacer (termed as Me-ARV771 and Me-MZ1) (Fig. 2F) to reversibly disrupts the interaction and abolish the protein degradation performance of the PROTAC. A reduction-inert ethylene glycol spacer was employed to synthesize the GSH-non-responsive control (namely Me-O-ARV771) (Supplementary Scheme 5, 6). Successful synthesis of the methacrylate-modified PROTACS was validated by nuclear magnetic resonance (^{1}H-NMR) and mass spectrometry (MS) measurements, respectively (Supplementary Figs. 13-17). High performance liquid chromatography (HPLC) examination displayed ARV771 was completely restored from Me-ARV771 upon 6.0 h incubation with dithiothreitol (DTT). In contrast, Me-O-ARV771 bearing ethylene glycol spacer kept stable throughout the experimental period (Fig. 2G and Supplementary Fig. 18), verifying superior reduction sensitivity of the disulfide bond-incorporated Me-ARV771.

With the reduction-activatable Me-ARV771 and Me-MZ1 in hand, we next sought to synthesize the POLY-PROTAC via PEG-induced RAFT copolymerization of Me-ARV771 (or Me-MZ1) and ionizable DPA monomer for intracellular acidity and reduction-triggered delivery of the BRD4 PROTACs. The resultant POLY-PROTACs were termed as PD7 (based on Me-ARV771) or PDM (based on Me-MZ1) according to the PROTAC molecular used. An MMP-2-cleavable GPLGLAG (GG) heptapeptide spacer was introduced into the PD7 POLY-PROTAC (namely PGD7) for prompting tumor-specific accumulation and cellular uptake of the POLY-PROTAC NPs (Supplementary Scheme 7, 8 and Figs. 19-24). Two MZ1-based POLY-PROTACs without GG peptide (PDM), and GG peptide spacer (PGDM) were also synthesized for comparison (Supplementary Scheme 9 and Figs. 25, 26). A reduction-insensitive POLY-PROTAC was also synthesized with Me-O-ARV771 (termed as PGDO7, Supplementary Scheme 12 and Fig. 31). All the synthesized POLY-PROTACs displayed well-controllable polymerization degrees and narrow molecular weight distribution as determined by ^{1}H-NMR and gel permeability chromatography measurements, respectively (Supplementary Table 1).

The POLY-PROTAC micellar NPs were then prepared via nanoprecipitation method as described previously[29–30]. At neutral pH of 7.4, dynamic light scattering (DLS) data and transmission electron microscopy (TEM) examinations revealed averaged hydrodynamic diameter of ~ 55 nm and spherical morphology of the POLY-PROTAC NPs with narrow particle size distribution (polydispersity index (PDI) < 0.2). In contrast, amorphous aggregates appeared at pH of 6.0 due to acid-induced protonation of DPA groups and dissociation of the POLY-PROTAC NPs (Figs. 2H, I).

To demonstrate acid-responsive property of the POLY-PROTAC NPs, we then synthesized Pheophorbide A (PPa, a fluorescence dye and well-studied photosensitizer)-labeled $mPEG_{113}$-GG-*b*-P(DPA_{50}-*r*-$HEMA_5$) (termed as PGDA) diblock copolymer via RAFT copolymerization (Supplementary Scheme 10, 11 and Figs. 27-30). The ARV771 or MZ1-conjugated POLY-PROTAC was then co-assembled with PGDA to obtain fluorophore-labeled POLY-PROTAC NPs. At neutral pH 7.4, the PPa-labeled POLY-PROTAC NPs displayed quenched fluorescence emission due to homo-fluorescence resonance energy transfer between PPa molecules[31]. On the contrary, the fluorescence emission was remarkably recovered at acidic pH of 6.2, mimicking the acidic microenvironment of the endosome organelles (pH = 5.8 ~ 6.5) (Fig. 2J). This phenomenon further validated acid-triggered dissociation of the POLY-PROTAC NPs, which might facilitate PROTAC release inside the tumor cells.

HPLC examination displayed that in the absence of GSH, ARV771 was marginally released from the PGD7 NPs at either neutral or acidic condition (i.e., pH = 7.4 or 6.0) (Fig. 2K). In contrast, ARV771 was remarkably restored with the addition of 10 mM GSH. For instance, over 50% of ARV771 was released upon 4 h incubation with 10 mM of GSH solution at pH of 6.0, which was ~20% higher than that determined at neutral pH. This phenomenon could be explained by the increased GSH accessibility when the POLY-PROTAC NPs was dissociated at acidic condition.

BRD4 degradation with the POLY-PROTAC NPs in vitro

To demonstrate the advantage of the MMP-2-sheddable POLY-PROTAC for increased cellular uptake and deep tumor penetration (Fig. 3A), the PGDA7 (with GG peptide spacer) and PDA7 (without GG peptide spacer) NPs were pre-treated with MMP-2 for 1 h to cleave the PEG corona as reported previously[32]. MDA-MB-231 breast tumor cells were then incubated with PDA7 or the dePEGylated PGDA7 NPs for the desired time durations. Flow cytometry measurement identified ~2.8-fold higher intracellular fluorescence signal of the PGDA7 group than the PDA7 one (Fig. 3B). Confocal laser scanning microscopy (CLSM) examination further revealed remarkably higher intracellular uptake of the PGDA7 NPs than the PDA7 control when examined at 12h incubation (Fig. 3C and Supplementary Fig. 32), validating that MMP-2-triggred dePEGylation prompted internalization of the POLY-PROTAC NPs.

The tumor penetration profile of the PPa-labeled POLY-PROTAC NPs was then investigated in three-dimensional (3D) multicellular spheroid (MCS) model of the MDA-MB-231 tumor *in vitro*. CLSM examination showed that upon 12h incubation, the MMP-2-insensitive PDA7 NPs were primarily entrapped in the peripheral area, and marginally penetrated into deep area of the MCSs (Figs. 3D, E). In contrast, the sheddable PGDA7 NPs highly diffused into the central area of the MCSs with ~ 3.0-fold higher fluorescence intensity at depth of 50 μm (Fig. 3F), implying remarkable tumor penetration profile of the sheddable POLY-PROTAC NPs.

With the MMP-2-liable POLY-PROTAC NPs in hand, we next evaluated their BRD4 degradation performance *in vitro*. Upon 24 h incubation, the GSH-activatable POLY-PROTACs of ARV771 and MZ1 efficiently reduced BRD4 protein in MDA-MB-231 tumor cells *in vitro* (Figs. 3G-J). In contrast, the PGDO7

POLY-PROTAC bearing ethylene glycol linker negligibly affected BRD4 expression (Fig. 3K), validating the crucial role of GSH-triggered reduction of the disulfide bond and restoration of the VHL ligand for protein degradation inside the tumor cells. MMP-2 pretreatment of the MMP-2-sheddable POLY-PROTAC NPs remarkably reduced the DC_{50} of the PGD7 and PGDM NPs, which were 1.9- and 3.1-fold lower the MMP-2-insensitive PD7 and PDM counterparts respectively, and comparable to that of the free ARV771 and MZ1 (Fig. 3L). This could be attributed to increased cellular uptake of the PGD7 and PGDM NPs upon MMP-2-mediated cleavage of the PEG corona (Supplementary Fig. 33).

Co-treatment with proteasome inhibitor MG132 abolished the protein degradation ability of the small molecular PROTACs (e.g., MZ1 and ARV771) and the POLY-PROTAC NPs (e.g., PGDM and PGD7) (Fig. 3M), verifying ubiquitin-proteasome-dependent BRD4 degradation profile of the POLY-PROTAC NPs. CCK-8 assay further revealed increased cytotoxicity of the PGDM and PGD7 NPs than that of the MMP-2 non-responsive PGDO7 control upon 72 h incubation (Fig. 3N). Collectively, above data demonstrated that the POLY-PROTAC NPs with sheddable PEG corona and reduction-liable linker efficiently degraded the POI and suppressed tumor cell proliferation *in vitro*.

Biodistribution and antitumor performance of the POLY-PROTAC NP in vivo

The tumor-specific accumulation and penetration of the POLY-PROTAC NPs was next investigated in MDA-MB-231 breast tumor-bearing BALB/c nude mouse model *in vivo*. The MMP-2-sheddable PGDA7 and their MMP-2-insensitive PDA7 analog NPs were administrated via intravenous (i.v.) injection at an identical ARV771 dose of 10 mg/kg and PPa dose of 5.0 mg/kg respectively when the tumor volume reached 200 mm^3. Fluorescence imaging *in vivo* displayed that both the PGDA7 and PDA7 NPs accumulated at the tumor site over time via passive tumor-targeting property of NPs (Fig. 4A). Noticeably, the PGDA7 NPs showed significantly higher intratumoral fluorescence intensity and slower decline than PDA7 at all the time points. For instance, the PGDA7 group was of 2.0-fold higher tumor fluorescence intensity than the PDA7 control at 36 h post-injection (Fig. 4B).

Tumor-specific distribution of the PGDA7 NPs was confirmed by fluorescence imaging of the major organs (e.g., heart, liver, spleen, lung and kidney) and the tumor tissue ex-vivo at 48 h post-injection (Fig. 4C). CLSM examination of the tumor section further illustrated that the PDA7 NPs distributed in the peripheral area of the blood vessels. In contrast, the PGDA7 NP diffused throughout the tumor tissue (Fig. 4D). Taken together, the fluorescence imaging and CLSM examination data verified increased tumor accumulation and penetration of the PGDA7 NPs due to MMP-2-mediated cleavage of the PEG corona.

We subsequently explored the anti-tumor efficacy of the POLY-PROTAC NPs in MDA-MB-231 tumor model *in vivo*. The tumor-bearing BLAB/c nude mice were randomly grouped when the tumor volume reached 100 mm^3 (n = 5), and i.v. injected with PBS, ARV771 or the PGD7 NP at an identified ARV771 dose of 10 mg/kg. The treatments were repeated every three days for five times (Fig. 4E). Free ARV771 marginally suppressed MDA-MB-231 tumor growth. In contrast, PGD7 NP significantly delayed ~ 50% of tumor growth and consequently elongated the survival of the tumor-bearing mice (Figs. 4F, G).

Immunohistochemistry (IHC) examination of the tumor section displayed that free ARV771 marginally affected BRD4 expression (Fig. 4I). In contrast, PGD7 NP remarkably suppressed BRD4 expression with ~ 4-fold lower BRD4-positive area than free ARV771 (Fig. 4J).

To elucidate the mechanism underlying the antitumor performance of the POLY-PROTAC NPs, BRD4 degradation in the tumor lysates was evaluated by western blot assay. Fig. 4K validated that the PGD7 NPs dramatically degraded BRD4 protein (Supplementary Fig. 34). Furthermore, PGD7 NP-treatment significantly elicited the expression of cleaved-caspase-3 both *in vitro* and *in vivo* (Fig. 4L), verifying BRD4 degradation induced apoptosis of the tumor cells since caspase-3 is a crucial executor of apoptosis[33]. BRD4 degradation-induced apoptosis of the tumor cells was further verified by Hematoxylin-eosin (H&E) staining of the tumor sections ex-vivo (Fig. 4H). There is no body weight loss was found during the whole experimental periods (Supplementary Fig. 35), and hematoxylin-eosin (H&E) staining of the major organs revealed negligible histopathological damage of the major organs (Supplementary Fig. 35), suggesting good biosafety of the POLY-PROTAC NPs.

Bioorthogonal click reaction amplified tumor distribution of the POLY-PROTAC NPs in vivo.

Insufficient tumor distribution of the PROTAC is one of the bottlenecks for PROTAC-based cancer therapy[2]. To further prompt tumor-specific accumulation of the POLY-PROTAC NPs (Fig. 5A), we next designed an extracellular tumor acidity-activatable pretargeted NP for tumor-specific delivery of the dibenzocyclooctyne (DBCO) groups. In parallel, azide groups were modified on the surface of the POLY-PROTAC NPs for in-situ bioorthogonal click reaction-amplified tumor accumulation and retention of the POLY-PROTAC NPs (Fig. 5A, see Supplementary Scheme 14 and Fig. 39 for synthesis of the N_3-PEG_{113}-GG-*b*-P(DPA_{50}-*r*-$HEMA_8$ diblock copolymer, termed as $N_{3@}$PGDH). The pretargeted NPs were prepared by self-assembly of DBCO-modified mPEG-*b*-poly(ethylene propyl amine) (namely PED) diblock copolymer (Supplementary Scheme 13 and Figs. 36, 37 for diblock copolymer synthesis).

The PED pretargeted NPs displayed homogeneous and spherical morphology with an averaged hydrodynamic diameter of ~ 60 nm at the neutral pH value (i.e., 7.4) (Fig. 5B), and dissociated dramatically at acidic pH (i.e., 6.5) mimicking the acidic tumor microenvironment (Fig. 5C). The PPa-conjugated PED NPs displayed quenched fluorescence at neutral condition (Supplementary Scheme 13 and Fig. 38). In contrast, the fluorescence of PPa recovered at pH value lower than 6.6 via extracellular acidity-induced dissociation of the pretargeted NPs (Fig. 5D), validating superior tumor extracellular acidity-responsive property of the pretargeted NPs.

To demonstrate extracellular acidity-triggered bioorthogonal click reaction, the DBCO-loaded PED pretargeted NP and the azide-modified N_3@PGD7 POLY-PROTAC NPs were incubated together at pH of 7.4 or 6.5, respectively. DLS examination showed uniform hydrodynamic diameter and narrow particle size distribution of the mixed pretargeted and POLY-PROTAC NPs in the FBS-containing neutral buffer solution (pH 7.4), suggesting negligible interaction between the PED and the N_3@PGD7 NPs since the DBCO groups were encapsulated inside the hydrophobic core of the PED NPs (Supplementary Fig. 40). In

contrast, DLS and TEM examination revealed the appearance of amorphous aggregates with broad size distribution at acidic pH of 6.5 (Figs. 5E, F). This phenomenon validated the bioorthogonal click reaction between the DBCO and azide groups to form cross-linked nanostructure between the PED copolymer and azide-functionalized POLY-PROTAC NPs.

We next sought to investigate whether bioorthogonal click reaction can increase intratumoral accumulation and retention of the POLY-PROTAC NPs *in vivo*. Fluorescence imaging *in vivo* displayed obvious fluorescence signal at the tumor site when the MDA-MB-231 tumor-bearing mice were i.v. injected with the PED pretargeted NPs (Fig. 5G), which was caused by tumor acidity-triggered dissociation of the PED NPs and activation of the PPa fluorescence signal via protonation of the EPA tertiary amine (Fig. 5G). CLSM examination of the tumor sections showed that the PED pretargeted NPs colocalized well with the cell membrane (labeled with wheat germ agglutinin, WGA) 2~4h post-injection, verifying that the PED NPs dissociated and exposed the DBCO groups in the extracellular matrix (ECM) of the tumor tissue (Fig. 5H). which could facilitate click reaction between the DBCO and azide groups presenting on the surface of the POLY-PROTAC NPs in the ECM.

To evaluate whether the in-situ click reaction enhance tumor accumulation of the PROTAC molecules *in vivo*, the N_3@PGD7 POLY-PROTAC NPs was i.v. administrated 2 h post-injection of the pretargeted NPs. Fluorescence imaging *in vivo* displayed much brighter fluorescence signal at the tumor site of the PED + N_3@PGDA7 group compared to the N_3@PGDA7-injected mouse group (Fig. 5I). For instance, PED + N_3@PGDA7 group showed ~ 2.0-fold higher fluorescence signal than the N_3@PGDA7 NP alone at 24-36h post-injection (Fig. 5K).

Increased tumor distribution of the POLY-PROTAC NPs was validated by fluorescence imaging of the major organs and tumor tissues ex-vivo 48 h post-injection (Fig. 5L). CLSM examination of the tumor sections demonstrated increased tumor accumulation and deep penetration of the N_3@PGDA7 POLY-PROTAC NPs when administrated post i.v. injection of the pretargeted PED NPs (Fig. 5J). HPLC examination of ARV771 distribution *in-vivo* further demonstrated increased intratumoral distribution and retention of the POLY-PROTAC NPs via in-situ click reaction. In comparison with free ARV771 and N_3@PGDA7 NPs, the combination of PED + N_3@PGDA7 NP remarkably enhanced tumor distribution of ARV771 by 3.9- and 1.9-fold respectively, when examined at 36 h post-injection (Fig. 5M). Both fluorescence imaging and HPLC data provided consistent evidence that the in-situ click reaction significantly enhanced tumor accumulation and retention of ARV771 PROTAC at the tumor site.

Bioorthogonal POLY-PROTAC NPs regressed breast tumor growth in vivo

Given significantly improved tumor distribution of the clickable POLY-PROTAC NPs, we next investigated their antitumor performance in MDA-MB-231 tumor model *in vivo* (Fig. 6A). Compared to free ARV771 or N_3@PGD7 NPs alone, the combination of the PED pretargeted and N_3@PGD7 NPs much more efficiently suppressed ~70% of MDA-MB-231 tumor growth (Fig. 6B), and elongated the survival of the tumor-bearing mice (Fig. 6C), which can be attributed to increased ARV771 distribution in the tumor tissue.

In previous studies, we had explored intracellular acidity-activatable PDT for circumventing multidrug resistance of the breast tumor[34]. To explore the potential of the POLY-PROTAC NPs as a generalizable nanoplatform for combinatory therapy, we next sought to combine the bioorthogonal NPs for PDT-enforced antitumor therapy (Fig. 6D). The N_3@PGDA7 NPs integrating the ARV771 POLY-PROTAC and PPa was prepared by co-assembling N_3@PGDH, PGD7 and PGDA diblock copolymers. Western blot assay displayed that combination of BRD4 degradation and PDT *in vitro* significantly activated the caspase-3 protein *in vitro*, implying cumulative antitumor performance of the N_3@PGDA7 NPs (Fig. 6E and Supplementary Figs. 41, 42).

The anti-tumor performance of combinatory PDT and BRD4 degradation was next investigated *in vivo*. The MDA-MB-231 tumor-bearing BALB/c nude mice were randomly grouped when the tumor volume reached ~ 100 mm^3 and treated with PBS, ARV771, PED + N_3@PGDA + Laser, PED + N_3@PGD7, PED + PGDA7 + Laser, or PED + N_3@PGDA7 + Laser, respectively (Fig. 6F). The N_3@PGDA7 NP was i.v. administrated 2h post-injection of the PED NP, and 671 nm laser irradiation was applied 36h post-injection of the N_3@PGDA7 NP. Fig. 6G demonstrated that PDT or ARV771 alone marginally suppressed proliferation of the MDA-MB-231 tumor. In contrast, the combination of the bioorthogonal NPs (PED + N_3@PGDA7) and PDT dramatically regressed 90% of tumor growth, 1.5-fold more efficient than BRD4 degradation alone by PED + N_3@PGDA7.

Furthermore, combination of the PED pretargeted NPs with N_3@PGDA7 and PDT elongated the survival of the tumor-bearing mice by 40% compared to that of the PED + N_3@PGDA7 group, with 40% animal survived in 100-days post treatment (Fig. 6H). TUNEL staining of the tumor sections revealed obvious apoptosis of the tumor cells in the PED + N_3@PGDA7 + PDT group, suggesting combination of PDT and BRD4 degradation with the bioorthogonal NPs cumulatively induced apoptosis of the tumor cells *in vivo* (Fig. 6J). Semi-quantitative analysis of the TUNEL staining data further revealed that PED + N_3@PGDA7 + Laser 15.2- and 4.2-fold more efficiently induced apoptosis of the tumor cells than ARV771 and PED + N_3@PGDA7, respectively (Supplementary Fig. 27). Treatment-induced apoptosis of the tumor cells was further confirmed by H&E staining of the tumor sections ex-vivo (Fig. 6K). Moreover, negligible body weight loss and histopathological damage of the major organs were observed during the experimental period, verifying satisfying biosafety of the POLY-PROTAC NPs (Fig. 6I and Supplementary Fig. 43).

IHC examination of the tumor tissue demonstrated significantly decreased BRD4 expression *in vivo* (Fig. 6L). Semi-quantitative analysis of the IHC images further determined that PED + N_3@PGDA7 2.6-fold more efficiently downregulated BRD4 expression than N_3@PGDA7 NP alone, validating increased intratumoral ARV771 distribution via the in-situ bioorthogonal reaction contributed to BRD4 degradation in *vivo* (Fig. 6M). Noticeably, the combination of PDT with PED + N_3@PGDA7 further promoted BRD4 degradation compared to PED + N_3@PGDA7 due to PDT-enhanced intracellular release of the ARV771 PROTAC in *vivo* (Figs. 6M, N). Noticeably, combinatory therapy by PED + N_3@PGDA7 + Laser 1.8- and 3.0-

fold more efficiently activated caspase-3 and degraded BRD4 than PED + N_3@PGD7, verifying synergistic apoptosis-induction profile between PDT and BRD4 degradation (Fig. 6O).

Conclusion

The heterobifunctional PROTACs with protein degradation ability has been recently investigated for cancer therapy[4]. However, clinical translation of the small molecular PROTACs severely suffers from their insufficient bioavailability and low tumor specificity. It remains one priority to develop novel PROTACs for tumor-specific protein degradation and minimizing the on-target but off-tumor adverse effects. A tumor-microenvironment-activatable POLY-PROTAC nanoplatform was thus engineered herein for tumor-specific delivery and potentiating antitumor performance of PROTACs.

In comparison with small molecular PROTAC counterparts, the POLY-PROTAC NPs possessed several distinct advantages for tumor-specific protein degradation and enhanced antitumor potency. First, the POLY-PROTAC NPs with MMP-2-liable PEG corona elongated blood circulation of the small molecular PROTACs, while the PEG corona was cleaved via intratumoral MMP-2 for facilitating tumor-specific ambulation and retention of the PROTACs. Second, the POLY-PROTAC NPs can be disintegrated in the intracellular acidic microenvironment. The PROTAC prodrug can thus be restored in the cytosol via GSH-mediated cleavage of the disulfide bond. Thirdly, the PROTAC encapsulation capacity of the POLY-PROTAC NPs can be readily tuned by adjusting the polymerization degree of PROTACs. Furthermore, we demonstrated that the POLY-PROTAC NPs can be adapted to bioorthogonal click reaction-enforced tumor-specificity of the POLY-PROTACs. Remarkably, the azide-modified POLY-PROTAC NPs showed 3.9-fold higher tumor accumulation than the small molecular counterpart via in-situ click reaction with the pretargeted NPs, and therefore further boost PROTAC-based cancer therapy. Last but not least, other kind of stimuli-activatable chemical bonds (e.g., thioketone, selenic or boric acid bond)[35, 36] can be utilized to achieve spatial-temporally PROTAC activation and reinforce the therapeutic performance.

In summary, a POLY-PROTAC prodrug strategy was developed for tumor-specific delivery of PROTAC in this study. We demonstrated for the first time that the extracellular MMP-2, intracellular acidity and reduction multiple stimuli-activatable POLY-PROTAC nanoplatform can achieve increased tumor accumulation, deep tumor penetration and enhanced protein degradation performance over the small molecular counterpart. The POLY-PROTAC nanoplatform with extracellular tumor acidity-triggered bioorthogonal click reaction remarkably enhanced tumor-specific PROTAC delivery. The clickable POLY-PROTAC nanoplatform can be further enforced with PDT for protein degradation and combinatory therapy, which completely eradicated the MDA-MB-231 TNBC tumor. Extracellular acidic and MMP-2 microenvironment has been well-documented in various solid tumors. Therefore, the acidity-activatable bioorthogonal POLY-PROTAC nanoplatform can be further extended for combinatory therapy of a broad spectrum of cancer by integrating multiple therapeutic regimens (e.g., chemotherapeutics and immunotherapeutics). Taken together, the ingenious POLY-PROTAC nanoplatform might provide a novel avenue for potentiating PROTAC-based cancer therapy.

Author Statement

J. Gao, H. Xu and H. Yu conceived the project and designed the study. Q. Zhu and X. Jiang synthesized the small molecule PROTACs and their methacrylate derivatives. J. Gao and B. Hou conducted the in-situ click reaction study. J. Gao synthesized the POLY-PROTACs and evaluated the protein degradation profiles *in vitro* and *in vivo*. J. Gao, L. Yang, Z. Zou and T. Wang conducted the anti-tumor study. J. Gao and H. Yu analyze the data and wrote the initial manuscript. T. Xu, Z. Xu and H. Xu revised the manuscript.

Declarations

Author statement

J. Gao, H. Xu and H. Yu conceived the project and designed the study. Q. Zhu and X. Jiang synthesized the small molecule PROTACs and their methacrylate derivatives. J. Gao and B. Hou conducted the in situ bioorthogonal click reaction study. J. Gao synthesized the POLYTACs and evaluated the protein degradation profiles *in vitro* and *in vivo*. J. Gao, L. Yang and Z. Zou conducted the anti-tumor study. J. Gao and H. Yu analyze the data and wrote the initial manuscript. Z. Xu, T. Xu and H. Xu revised the manuscript.

Supporting Information

Supporting Information is available from the author.

Acknowledgements

This work was supported by the National Natural Science Foundation of China (51873228, 22074043), International Cooperation Project of Science and Technology Commission of Shanghai Municipality (20430711800), the Youth Innovation Promotion Association of CAS (2014218), and Open Funds of State Key Laboratory of Drug Research, Shanghai Institute of Materia Medica, CAS (SIMM2105KF-12). The Mass Spectrometry System and the cell sorter BD Influx of the National Facility for Protein Science in Shanghai (NFPS), Shanghai Advanced Research Institute, CAS are gratefully acknowledged. All animal procedures were carried out under the guidelines approved by the Institutional Animal Care and Use Committee (IACUC) of the Shanghai Institute of Materia Medica, CAS.

Conflict of Interest

The authors declare no conflict of interest

References

1. Lai, A. C. & Crews, C. M. Induced Protein Degradation: an Emerging Drug Discovery Paradigm. *Nat. Rev. Drug Discov.* **16**, 101-114 (2017).

2. Dale, B. *et al.* Advancing Targeted Protein Degradation for Cancer Therapy. *Nat. Rev. Cancer* **21**, 638-654 (2021).

3. Chamberlain, P. P. & Hamann, L. G. Development of Targeted Protein Degradation Therapeutics. *Nat. Chem. Biol.* **15**, 937-944 (2019).

4. Pettersson, M. & Crews, C. M. PROteolysis TArgeting Chimeras (PROTACs)-Past, Present and Future. *Drug Discov. Today* **31**, 15-27 (2019).

5. Skaar, J. R., Pagan, J. K. & Pagano, M. SCF Ubiquitin Ligase-Targeted Therapies. *Nat. Rev. Drug Discov.* **13**, 889-903 (2014).

6. Sakamoto, K. M. *et al.* Protacs: Chimeric Molecules that Target Proteins to the Skp1–Cullin–F Box Complex for Ubiquitination and Degradation. *Proc. Natl Acad. Sci. USA* **98**, 8554 (2001).

7. Burslem, G. M. & Crews, C. M. Proteolysis-Targeting Chimeras as Therapeutics and Tools for Biological Discovery. *Cell* **181**, 102-114 (2020).

8. Backus, K. M. *et al.* Proteome-Wide Covalent Ligand Discovery in Native Biological Systems. *Nature* **534**, 570-574 (2016).

9. Popovic, D., Vucic, D. & Dikic, I. Ubiquitination in Disease Pathogenesis and Treatment. *Nat. Med.* **20**, 1242-1253 (2014).

10. Schapira, M., Calabrese, M. F., Bullock, A. N. & Crews, C. M. Targeted protein degradation: expanding the toolbox. *Nat. Rev. Drug Discov.* **18**, 949-963 (2019).

11. Neklesa, T. K., Winkler, J. D. & Crews, C. M. Targeted Protein Degradation by PROTACs. *Pharmacol Ther* **174**, 138-144 (2017).

12. Bushweller, J. H. Targeting Transcription Factors in Cancer-from Undruggable to Reality. *Nat. Rev. Cancer* **19**, 611-624 (2019).

13. Raina, K. *et al.* PROTAC-induced BET Protein Degradation as a Therapy for Castration-Resistant Prostate Cancer. *Proc. Natl Acad. Sci. USA* **113**, 7124-7129 (2016).

14. Lu, J. *et al.* BRD4 Degradation By Protacs Represents a More Effective Therapeutic Strategy Than BRD4 Inhibitors in DLBCL. *Blood* **126**, 2050-2050, (2015).

15. Moreau, K. *et al.* Proteolysis-Targeting Chimeras in Drug Development: A safety perspective. *Br J Pharmacol* **177**, 1709-1718 (2020).

16. Reynders, M. *et al.* PHOTACs Enable Optical Control of Protein Degradation. *Sci. Adv.* **6**, eaay5064 (2020).

17. Cotton, A. D., Nguyen, D. P., Gramespacher, J. A., Seiple, I. B. & Wells, J. A. Development of Antibody-Based PROTACs for the Degradation of the Cell-Surface Immune Checkpoint Protein PD-L1. *J Am Chem Soc* **143**, 593-598 (2021).

18. Pillow, T. H. *et al.* Antibody Conjugation of a Chimeric BET Degrader Enables in vivo Activity. *ChemMedChem* **15**, 17-25 (2020).

19. Banik, S. M. *Nature* **584** (2020).

20. Maneiro, M. A. *et al.* Antibody-PROTAC Conjugates Enable HER2-Dependent Targeted Protein Degradation of BRD4. *ACS Chem. Biol.* **15**, 1306-1312 (2020).

21. Liu, J. *et al.* Cancer Selective Target Degradation by Folate-Caged PROTACs. *J Am Chem Soc* **143**, 7380-7387 (2021).

22. He, S. *et al.* Aptamer-PROTAC Conjugates (APCs) for Tumor-Specific Targeting in Breast Cancer. *Angew. Chem. Int. Ed.*, (2021).

23. Xue, G., Wang, K., Zhou, D., Zhong, H. & Pan, Z. Light-Induced Protein Degradation with Photocaged PROTACs. *J Am Chem Soc* **141**, 18370-18374 (2019).

24. Liu, J. *et al.* Light-induced Control of Protein Destruction by Opto-PROTAC. *Sci. Adv.* **6**, eaay5154 (2020).

25. Hou, B. *et al.* Engineering Stimuli-Activatable Boolean Logic Prodrug Nanoparticles for Combination Cancer Immunotherapy. *Adv. Mater* **32**, e1907210 (2020).

26. Zhou, F. *et al.* Engineering Chameleon Prodrug Nanovesicles to Increase Antigen Presentation and Inhibit PD-L1 Expression for Circumventing Immune Resistance of Cancer. *Adv. Mater* **33**, 2102668 (2021).

27. Wang, Y. *et al.* A Nanoparticle-Based Strategy for the Imaging of a Broad Range of Tumours by Nonlinear Amplification of Microenvironment Signals. *Nat Mater* **13**, 204-212 (2014).

28. Yang, B., Gao, J., Pei, Q., Xu, H. & Yu, H. Engineering Prodrug Nanomedicine for CancerImmunotherapy. *Adv Sci* **7**, 2002365 (2020).

29. Riley, R. S., June, C. H., Langer, R. & Mitchell, M. J. Delivery Technologies for Cancer Immunotherapy. *Nat. Rev. Drug Discov.* **18**, 175-196 (2019).

30. Ma, X. *et al.* Ultra-pH-Sensitive Nanoprobe Library with Broad pH Tunability and Fluorescence Emissions. *J Am Chem Soc* **136**, 11085-11092 (2014).

31. Wang, Y. *et al.* Disulfide Bond Bridge Insertion Turns Hydrophobic Anticancer Prodrugs into Self-assembled Nanomedicines. *Nano Lett* **14**, 5577-5583 (2014).

32. Feng, B. *et al.* Binary Cooperative Prodrug Nanoparticles Improve Immunotherapy by Synergistically Modulating Immune Tumor Microenvironment. *Adv. Mater* **30**, 1803001 (2018).

33. Wang, W. *et al.* In situ Activation of Therapeutics Through Bioorthogonal Catalysis. *Adv Drug Deliv Rev* **176**, 113893 (2021).

34. Qin, H. *et al.* Development of a Cancer Vaccine Using In Vivo Click-Chemistry-Mediated Active Lymph Node Accumulation for Improved Immunotherapy. *Adv. Mater* **33**, 2006007 (2021).

35. Wang, H. *et al.* Metabolic Labeling and Targeted Modulation of Dendritic Cells. *Nat Mater* **19**, 1244-1252 (2020).

36. Bai, L. *et al.* Targeted Degradation of BET Proteins in Triple-Negative Breast Cancer. *Cancer Res* **77**, 2476-2487 (2017).

37. Donati, B., Lorenzini, E. & Ciarrocchi, A. BRD4 and Cancer: Going Beyond Transcriptional Regulation. *Molecular Cancer* **17**, 164 (2018).

38. Cochran, A. G., Conery, A. R. & Sims, R. J., 3rd. Bromodomains: a New Target Class for Drug development. *Nat. Rev. Drug Discov.* **18**, 609-628 (2019).

39. Wang, D. *et al.* Acid-Activatable Versatile Micelleplexes for PD-L1 Blockade-Enhanced Cancer Photodynamic Immunotherapy. *Nano Lett* **16**, 5503-5513 (2016).

40. Wang, T. *et al.* Intracellularly Acid-Switchable Multifunctional Micelles for Combinational Photo/Chemotherapy of the Drug-Resistant Tumor. *ACS Nano* **10**, 3496-3508 (2016).

41. Liu, J., Chen, Q., Feng, L. & Liu, Z. Nanomedicine for Tumor Microenvironment Modulation and Cancer Treatment Enhancement. *Nano Today* **21**, 55-73 (2018).

42. Zhou, F. *et al.* Tumor Microenvironment-Activatable Prodrug Vesicles for Nanoenabled Cancer Chemoimmunotherapy Combining Immunogenic Cell Death Induction and CD47 Blockade. *Adv. Mater* **31**, 1805888 (2019).

43. Piya, S. *et al.* BRD4 Proteolysis Targeting Chimera (PROTAC) ARV-825, Causes Sustained Degradation of BRD4 and Modulation of Chemokine Receptors, Cell Adhesion and Metabolic Targets in Leukemia Resulting in Profound Anti-Leukemic Effects. *Blood* **128**, 748-748 (2016).

44. Song, R. *et al.* Acidity-Activatable Dynamic Nanoparticles Boosting Ferroptotic Cell Death for Immunotherapy of Cancer. *Adv. Mater* **33**, 2101155 (2021).

45. Feng, B. *et al.* Self-Amplified Drug Delivery with Light-Inducible Nanocargoes to Enhance Cancer Immunotherapy. *Adv. Mater* **31**, 1902960 (2019).

Figures

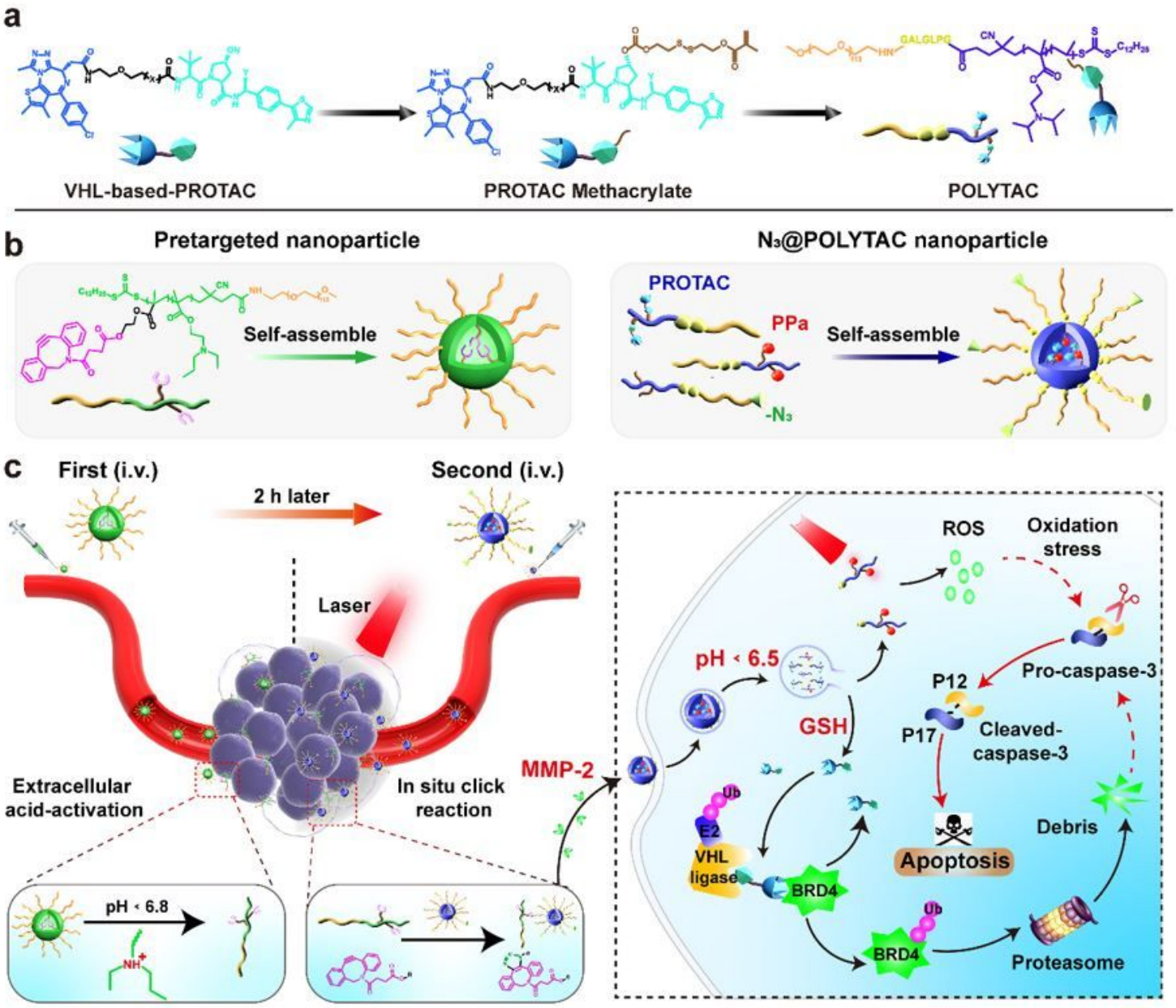

Figure 1

Schematic illustration of tumor microenvironment-activatable POLYTAC nanoparticles for bioorthogonal click reaction-enhanced cancer therapy. a, Synthesis of POLYTAC via RAFT polymerization approach, the PROTAC molecule was modified with disulfide linker and thereafter copolymerized with DPA using a MMP-2-liable macromolecular chain transfer agent; **b,** Self-assemble of the BDCO-conjugated pretargeted nanoparticles, and the azide-modified POLYTAC nanoparticles; **c,** Schematic demonstration of bioorthogonal strategy-promoted tumor distribution and combinatory tumor therapy with the POLYTAC nanoparticles, which displayed enhanced tumor distribution and deep penetration through in-situ click reaction with the pretargeted nanoparticles and deshielding of the PEG corona in the extracellular matrix

of tumor. The POLYTAC nanoparticles were then internalized with the tumor cells for BRD4 degradation and combinatory cancer therapy with PDT.

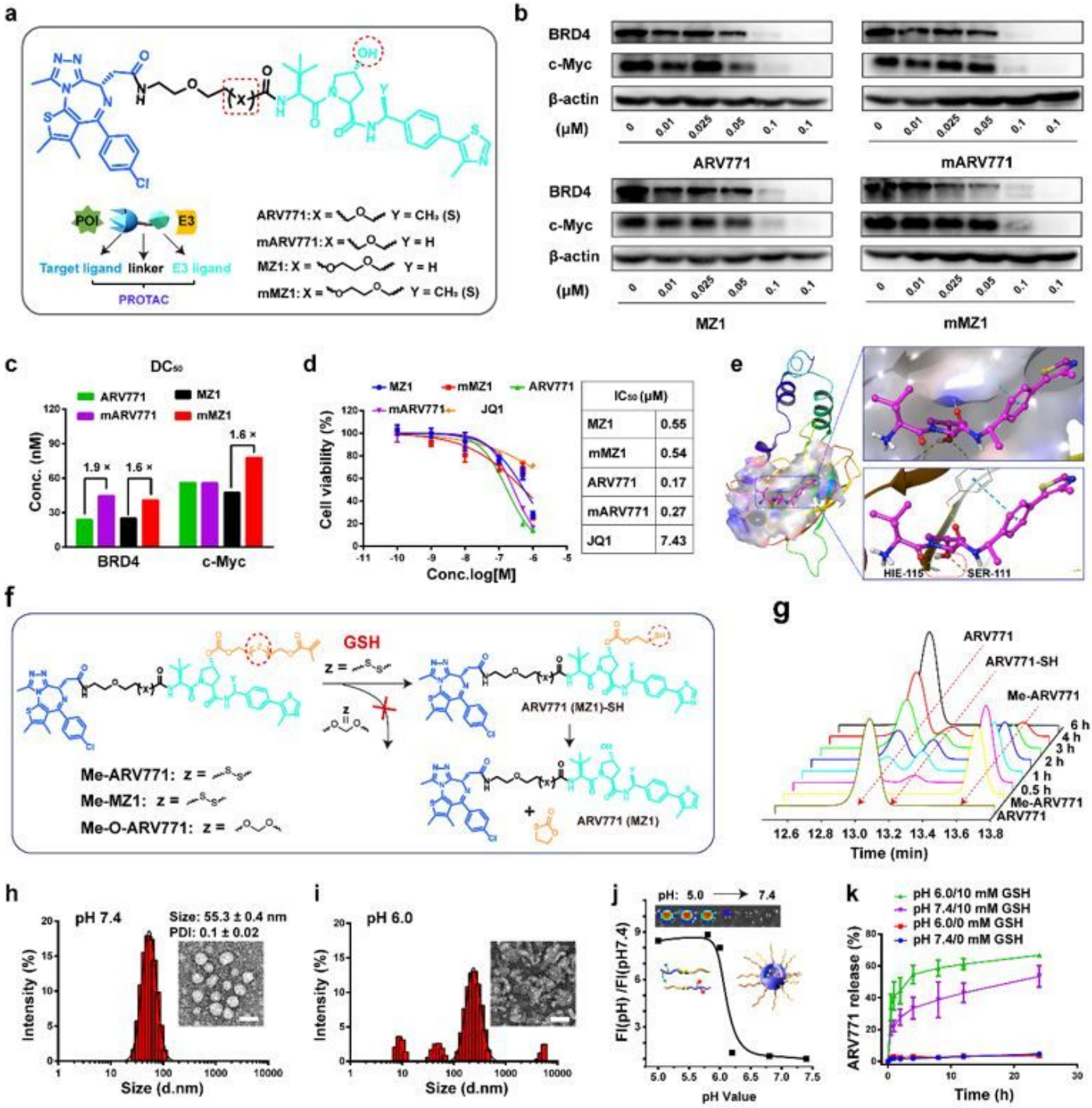

Figure 2

Synthesis and characterization of the PROTAC prodrug. a, Synthesis of BRD4-targeted VHL PROTACs; **b,** Western blot assay of PROTAC-mediated BRD4 degradation and c-Myc downregulation in the MDA-MB-231 breast tumor cells after 24 h incubation; **c,** Western blot assay- determined half BRD4 degradation concentration (DC_{50}) of the PROTACS; **d,** PROTACs efficiently inhibited proliferation of MDA-MB-231 cell

in a dose-dependent manner *in vitro* (insert showed the IC_{50} of the indicated PROTACs and JQ1). The cells were incubated with the PROTACs or JQ1 for 72 h before subjected to CCK-8 assay; **e,** Molecular docking of VHL ligand (purple) binding with the VHL protein. The panorama (left) and detailed drawing (right) of dock; **f,** Schematic illustration of GSH-mediated activation of ARV771 from the Me-ARV771; **g,** HPLC plots of reduction-triggered ARV771 restoration via co-incubation with 5.0 mM of DTT; **h, i,** Representative DLS data and TEM images of the PGD7 nanoparticle at (**h**) pH 7.4, or (**i**) pH 6.0; (**j**) Acid-activatable fluorescence profile of the PPa-labled PGDA7 nanoparticles (the fluorescence intensity was normalized with that determined at pH 7.4 (insert showed the fluorescence image of the PGDA7 nanoparticle suspensions at different pHs); **k,** GSH-triggered ARV771 release from the PGD7 nanoparticle at pH 7.4 or pH of 6.0 (with or without 10 mM GSH addition).

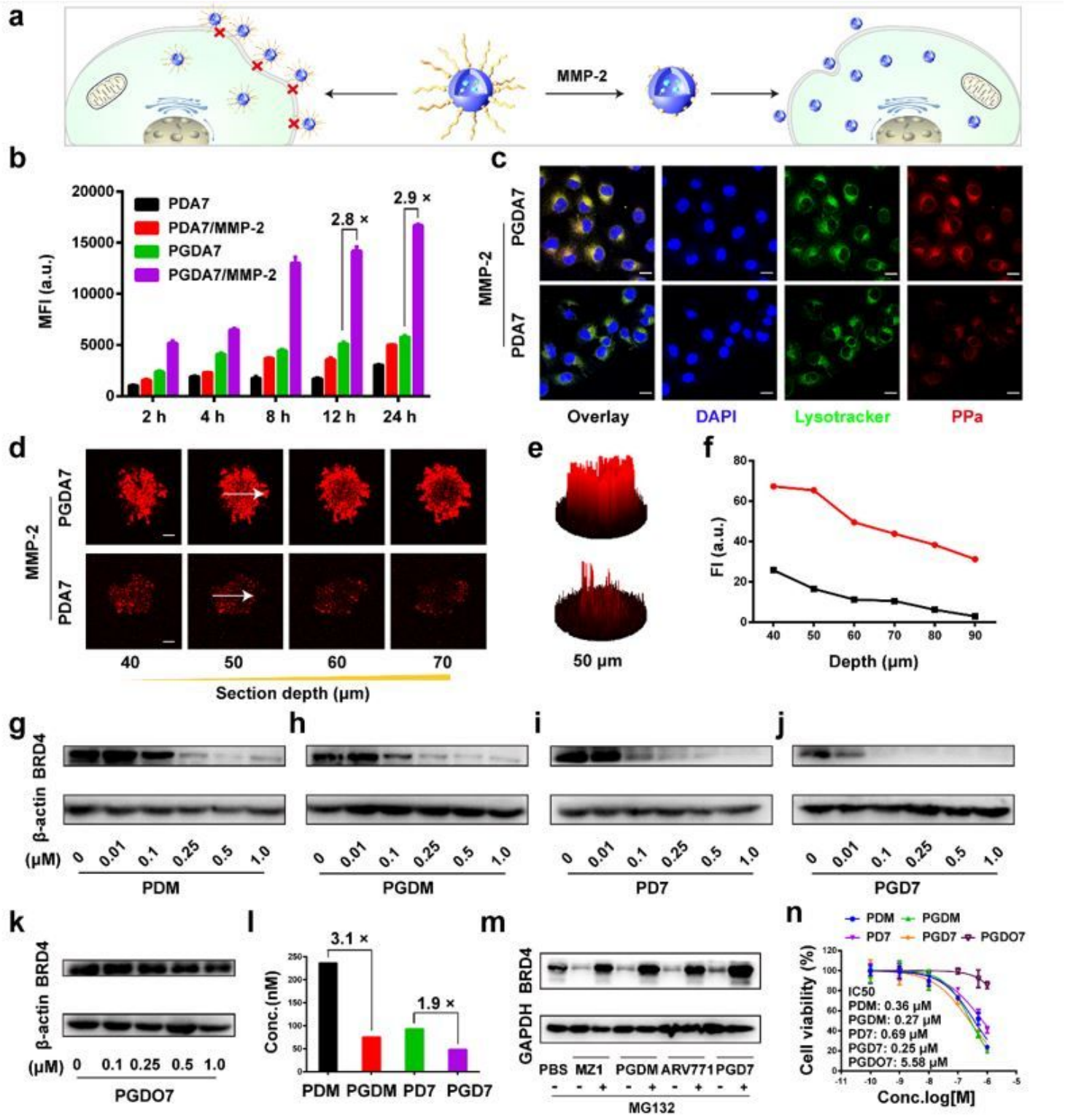

Figure 3

Cellular uptake, tumor penetration and BRD4 degradation performance of the sheddable POLYTAC nanoparticle *in vitro*. **a,** Cartoon illustration of MMP-2-triggered cleavage of the PEG corona and increased cellular uptake of the PGD7 nanoparticles *in vitro*; **b,** Flow cytometric analysis of cellular uptake of PGDA7 and PDA7 nanoparticles in *vitro* (The nanoparticles were pre-treated with 0.2 mg/mL of MMP-2 for 1h); **c,** CLSM examination of intracellular distribution of the POLYTAC nanoparticles upon 12 h

incubation (scale bar = 20 μm); **d-f,** MMP-2-responsive PGDA7 nanoparticles displayed increased penetration ability in the MCSs of MDA-MB-231 cells *in vitro* than the MMP-2-non-resposive PDA7 counterpart. (**d**) CLSM examination of PGDA7 and PDA7 nanoparticle distribution post 12 h incubation *in vitro*; (**e**) 2.5-D reconstruction of the CLSM images at a depth of 50 μm; (**f**) Fluorescence intensity of the central region versus Z-axis depth; **g-j,** The reduction-activatable POLYTAC nanoparticle efficiently degraded BRD4 protein in the MDA-MB-231 cells *in vitro*. (**h-j**) Western blot assay of BRD4 degradation in MDA-MB-231 cells with various GSH-sensitive POLYTAC nanoparticles *in vitro* upon 24 h incubation; **k,** Western blot assay of BRD4 expression in the PGDO7 nanoparticle-treated MDA-MB-231 cells *in vitro*; **l,** DC_{50} of the POLYTAC nanoparticles for degrading BRD4 in the MDA-MB-231 cells *in vitro*; **m,** POLYTAC nanoparticle degraded POI via the ubiquitin-proteasome system, western blot assay of BRD4 expression in the MDA-MB-231 cell with or without MG132 incubation (MZ1/ARV771 concentration of 1.0 μM and MG132 concentration of 5.0 mM, respectively); **n,** PGDM and PGD7 nanoparticles efficiently inhibited the proliferation of MDA-MB-231 cells *in vitro* (The POLYTAC nanoparticle were named according to the PROTAC and components integrated, P: PEG chain; G: MMP-2-liable GPLGLAG spacer; D: acid-activatable DPA groups; 7: disulfide bond-bearing ARV771 methacrylate; M: disulfide bond-bearing MZ1 methacrylate; O7: ethylene group-bearing ARV771 methacrylate; A: Pyropheophorbide a, PPa).

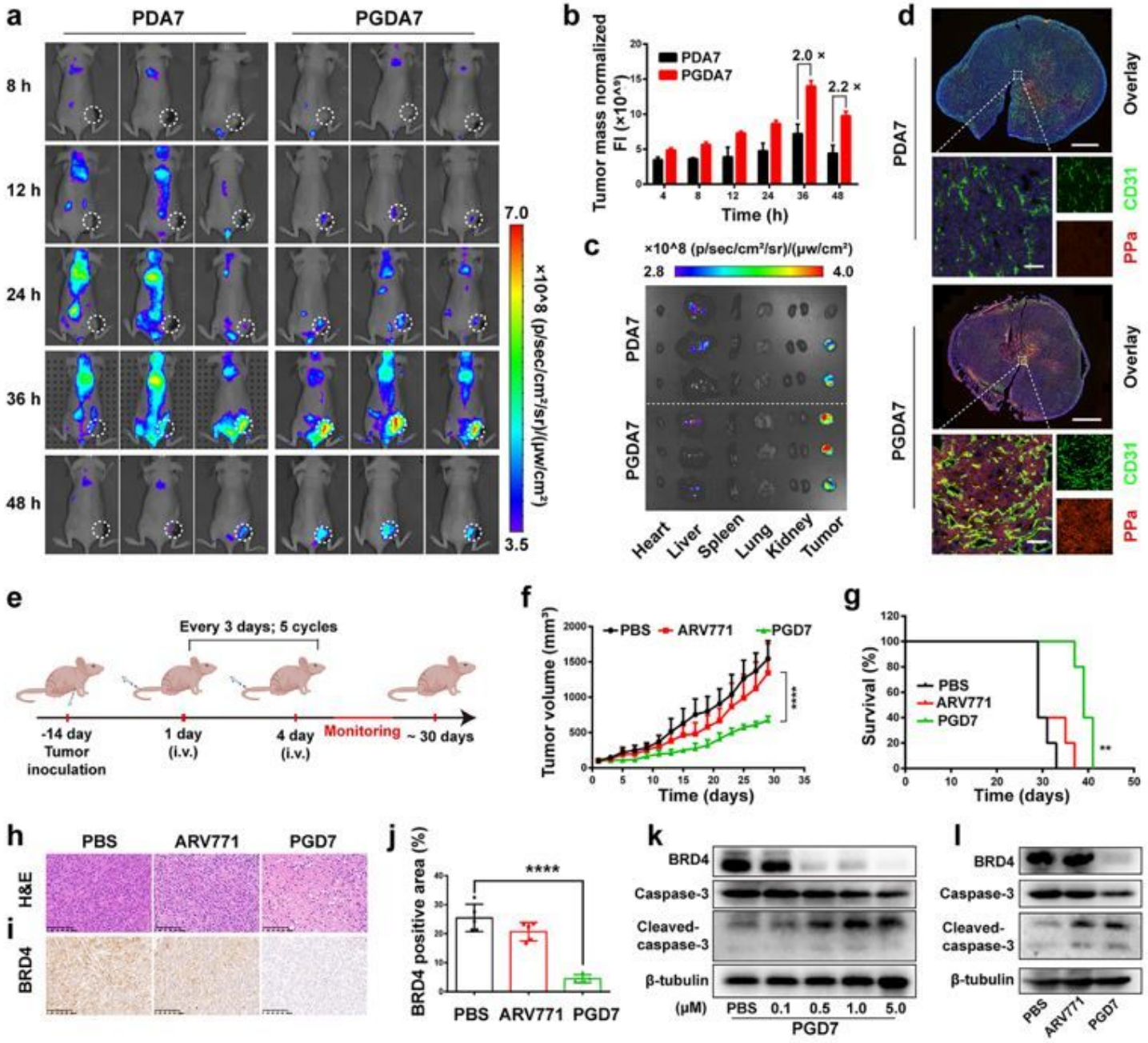

Figure 4

Biodistribution and anti-tumor performance of the POLYTAC nanoparticles *in vivo*. a, Fluorescence images of POLYTAC nanoparticle distribution in MDA-MB-231 tumor-bearing nude mice *in vivo*, the MMP-2-activatible PGDA7 nanoparticle specifically accumulated at the tumor site *in vivo*; **b,** Normalized fluorescence intensities of the tumor tissue, and (**c**) Fluorescence images of the major organs and the tumor tissue ex-vivo (the major organs and tumors were harvested 48 h post-injection); **d,** CLSM images of ex-vivo tumor sections at 48 h post-injection (top panel scale bar = 2.0 mm, bottom panel scale bar = 50 μm); **e,** Treatment schedule of POLYTAC nanoparticle-performed antitumor study in MDA-MB-231 tumor-bearing nude mice; **f-g**, PGD7 nanoparticle efficiently suppressed MDA-MB-231 tumor growth without obvious adverse effect. (**f**) Tumor growth curves, and (**g**) survival plots of the tumor-bearing

Balb/c nude mice upon Poly-PROTAC nanoparticle treatments (n = 5); **h,** H&E staining of the tumor sections at the end of antitumor study (scale bar = 100 μm); **i-l,** The PGD7 nanoparticles degraded BRD4 protein and activated caspase-3 in the tumor cell *in vitro* and *in vivo*. (**i**) IHC staining of BRD4 expression in the tumor sections ex-vivo (scale bar = 100 μm), and (**j**) Semi-quantitative analysis of IHC-determined BRD4 expression; **k&l**, Western blot assay of PGD7 POLYTAC-induced BRD4 degradation and caspase-3 activation in MDA-MB-231 tumor cells (**k**) *in vitro*, and (**l**) *in vivo* (the tumors were harvested at the second day post five-cycles treatments).

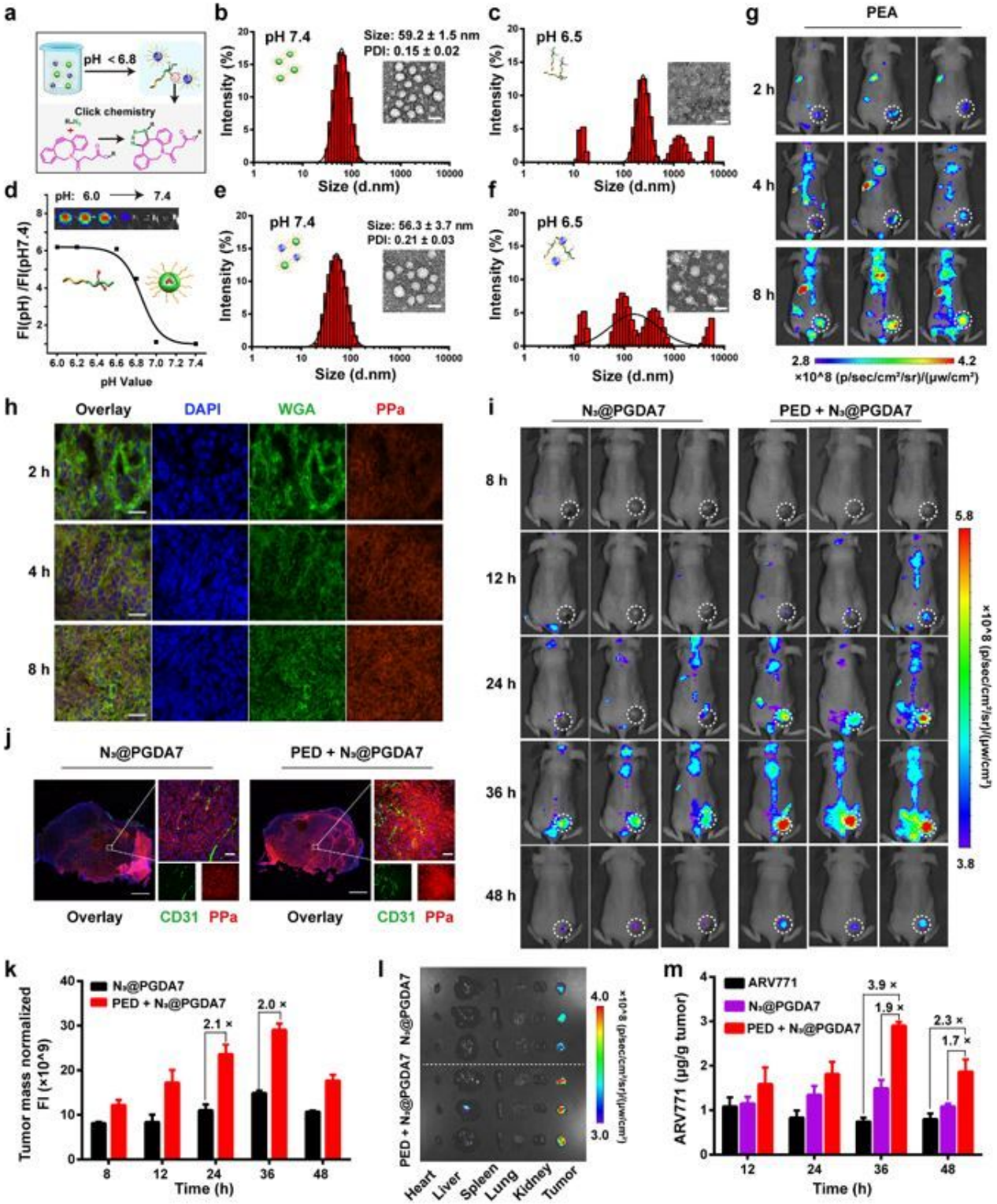

Figure 5

Bioorthogonal click reaction improved tumor accumulation of the POLYTAC nanoparticle *in vivo*. a, Diagrammatic illustration of tumor-specific delivery of the POLYTAC nanoparticles via bioorthogonal click reaction with the extracellular tumor acidity-activatable pretargeted nanoparticles; **b-d,** DLS and TEM examination of the pretargeted nanoparticles at (**b**) pH 7.4, and (**c**) pH 6.5. The PED pretargeted nanoparticles dissociated at the extracellular tumor acidity for release DBCO *in vitro*; (**d**) Normalized fluorescence plots of the pretargeted nanoparticle versus pH values (insert: fluorescence image of the PEA nanoparticle at different pH conditions); **e, f,** DLS and TEM examination of the particle distribution and morphology of the mixture of PED + N_3@PGD7 nanoparticles at (**e**) pH 7.4, and (**f**) 6.5. The bioorthogonal reaction occurred between the PED pretargeted nanoparticles and the N_3@PGD7 POLYTAC nanoparticles at pH 6.5; **g, h,** The pretargeted nanoparticles specifically accumulated at the tumor site and were activated with the tumor acidic pH; (**g**) Fluorescence imaging of biodistribution of the PED nanoparticle in the MDA-MB-231 tumor bearing nude mice *in vivo*, and (**h**) CLSM examination the tumor section ex-vivo (scale bar = 50 μm); **i-m,** The PED nanoparticles increased tumor distribution of the N_3@PGD7 nanoparticles via bioorthogonal click reaction *in vivo*; (**i**) Fluorescence imaging of MDA-MB-231 tumor-bearing Balb/c nude mice, and (**j**) CLSM images of the tumor sections at 48 h post-injection (scale bar = 50 μm) (The mice were i.v. injected with the PED pretargeted nanoparticles at a DBCO dose of 1.0 mg/kg, and subsequently i.v. injected with the N_3@PGDA7 nanoparticles at an azide dose of 0.055 mg/kg 2h post PED injection); The in-situ bioorthogonal click reaction remarkably increased ARV771 distribution in the tumor, (**k**) Intratumoral fluorescence intensity of N_3@PGDA7 nanoparticle-injected mice, and (**l**) Fluorescence imaging of the major organs 48 h post-injection; **m**) HPLC-determined intratumoral ARV771 distribution.

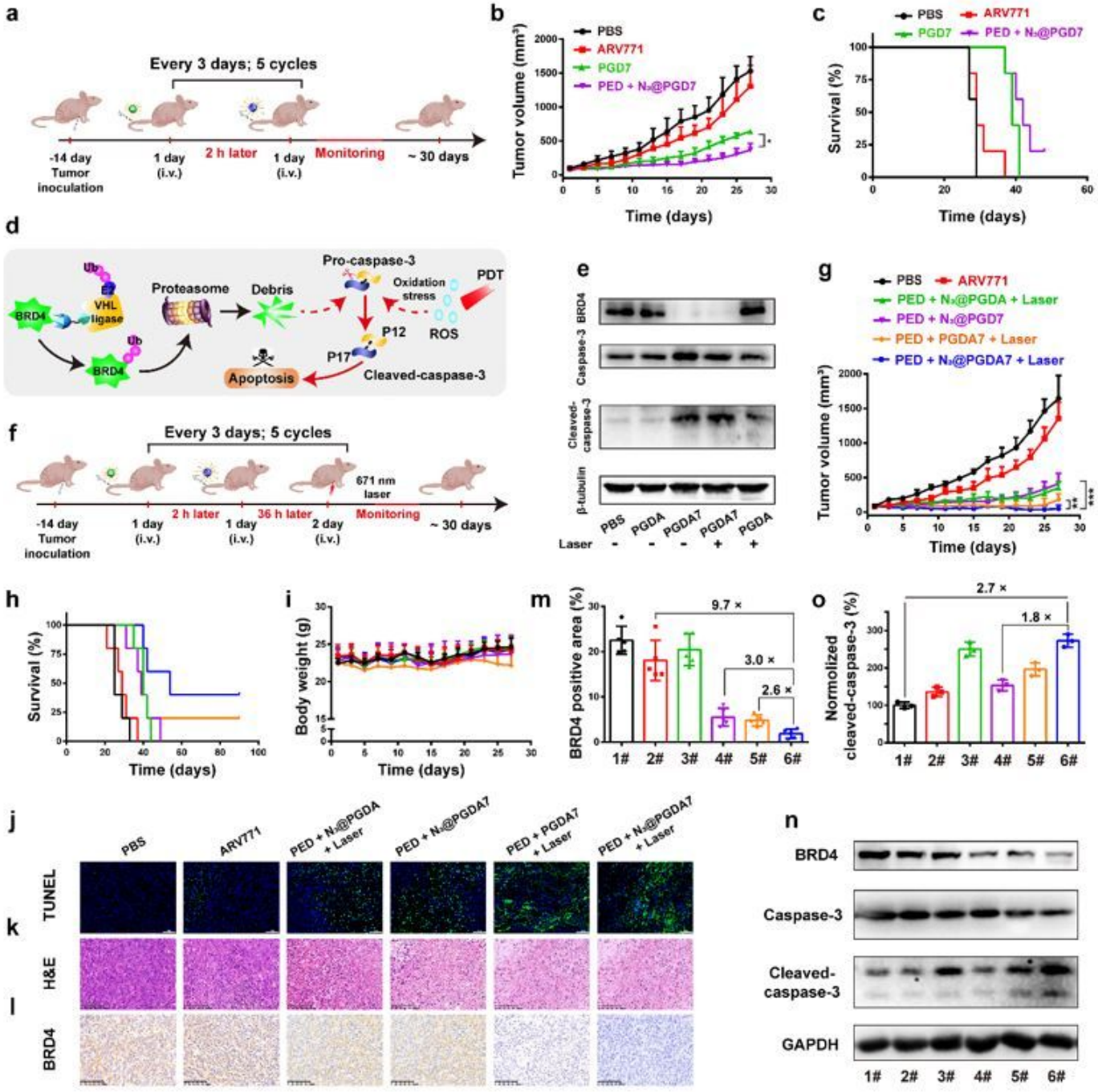

Figure 6

Anti-tumor performance of the bioorthogonal POLYTAC nanoparticle via BRD4 degradation and PDT. **a,** Experimental design for bioorthogonal POLYTAC nanoparticle-based anti-tumor study; **b,** Averaged tumor growth curves after treating with various formulations (PBS, ARV771, PGD7 and PED + N_3@PGD7, n = 5); **c,** Survival curves of the tumor-bearing mice; **d,** Schematic illustration of the bioorthogonal nanoparticle-based combinatory therapy of TNBC tumor via BRD4 degradation and caspase-3 activation in the tumor *in vivo*; **e,** The combination of ARV771 and PDT cumulatively activated caspase-3 of the tumor cells *in vivo*. Western blot assay of the tumor lysates upon different treatments; **f,** Experimental schedule of bioorthogonal POLYTAC nanoparticle-performed combinatory therapy in MDA-MB-231 xenograft tumor

model; **g,** Averaged tumor growth curves after treatment with various formulations (PBS, ARV771, PED + N_3@PGDA + Laser, PED + N_3@PGD7, PED + PGD7 + Laser, PED + N_3@PGDA7 + Laser, n = 5，irradiation condition: 400 mW/cm^2, 5.0 min); **h,** Survival curves, and **i,** Body weight change of the tumor-bearing mice monitored during the experimental period; **j,** TUNEL (blue: DAPI, green: apoptotic cell), and (**k**) H&E staining of the tumor section 30-days post-treatment (scale bar = 100 μm); **l,** IHC analysis, and m) Semi-quantitated BRD4 expression in the tumor tissues; **n,** Western blot assay, and (**o**) Normalized expression of the activated caspase-3 in the tumor lysates (1#: PBS; 2#: ARV771; 3#: PED + N_3@PGDA + Laser; 4#: PED + N_3@PGD7; 5#: PED + PGD7 + Laser; 6#: PED + N_3@PGDA7 + Laser).

Supplementary Files

This is a list of supplementary files associated with this preprint. Click to download.

- SIGJ20211222Final.docx